RESEARCH ARTICLE

Geometric descriptors for the prediction of snowflake drag

Kilian Köbschall[1] · Jan Breitenbach[1] · Ilia V. Roisman[1] · Cameron Tropea[1] · Jeanette Hussong[1]

Abstract

The dynamics of solid particles of complex shapes such as airborne snowflakes are governed by aerodynamic drag forces that are a function of the relative velocity of the particle in the flow and the particle drag coefficient, which depends on the particle geometry and its orientation. In this study, artificial snowflakes are produced by additive manufacturing and their drag coefficients are obtained by measuring the terminal velocity in a liquid container, matching the Reynolds number typically encountered in natural occurrences. The experimental results show that the convex hull of the particle is suitable to accurately predict the drag force with existing correlations. Since it is unfeasible to accurately measure the three-dimensional geometries of natural snowflakes, the approximation with the convex hull provides a useful simplification. Furthermore, the known shapes of the artificial snowflakes are used to develop correlations to estimate the most relevant three-dimensional descriptors to predict the drag of snowflakes from a two-dimensional projection onto an arbitrary plane.

Graphic abstract
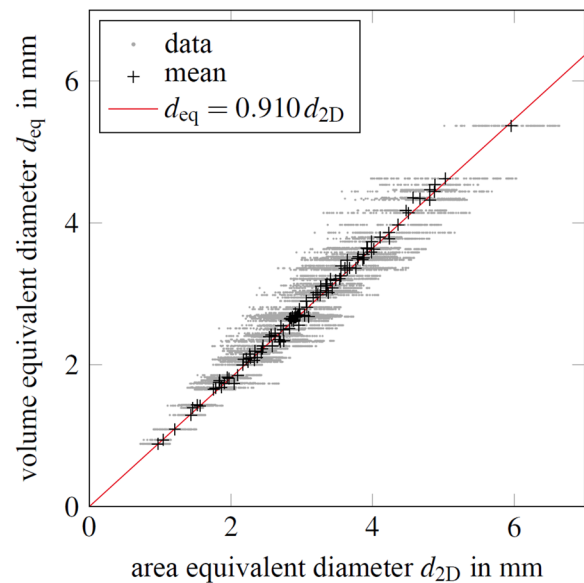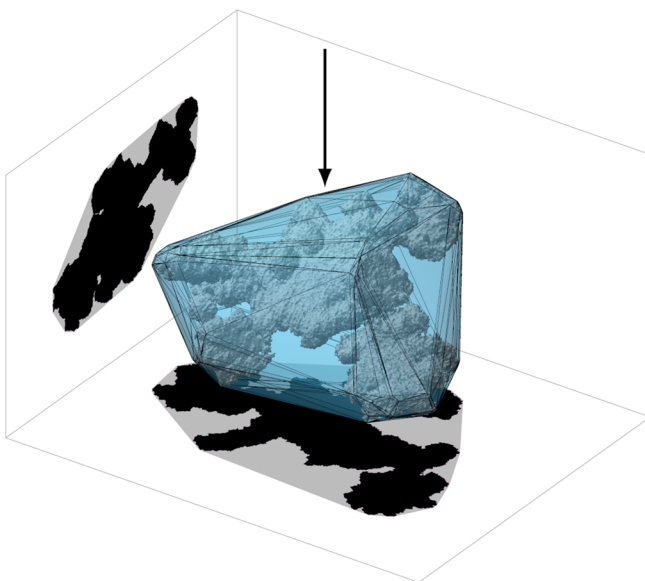
1 Introduction

For computationally based weather predictions or ice accretion phenomena, the dynamics of a single ice crystal or snowflake have to be accurately described (Saunders and Peck 1998; Farzaneh 2008; Currie et al. 2012). However, this problem is not trivial since in many cases atmospheric particles assume very different, complex shapes. Figure 1

✉ Kilian Köbschall
koebschall@sla.tu-darmstadt.de

1   Institute of Fluid Mechanics and Aerodynamics, Technische
     Universität Darmstadt, Alarich-Weiss-Strasse 10,
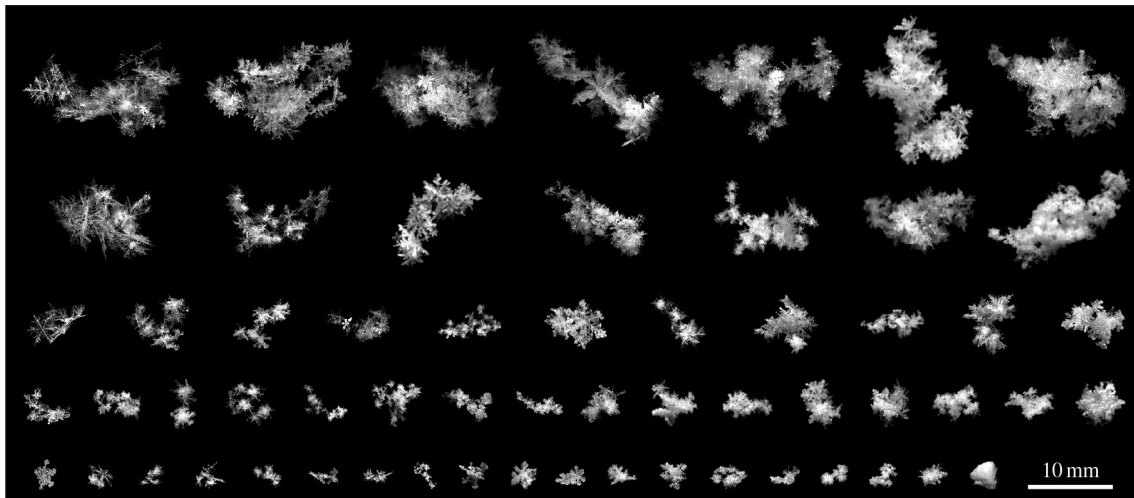   64287 Darmstadt, Germany

Fig. 1 Photographs of natural snowflakes captured using a high-resolution camera. Exemplary images from the database of Grazioli et al. (2021)

shows examples of natural snowflakes during free fall recorded with a stereographic camera system, as described by Garrett et al. (2012) and Pilcher (2013).

The dynamics of natural snowflakes are mainly characterized by their relative velocity U, apparent size and form, particle orientation (which determine the drag force vector F_d) and their particle mass m. These parameters can strongly vary as shown by Langleben, who determined the terminal velocity of snowflakes and ice crystals for various particle masses (Langleben 1954). Data on fall speeds, corresponding average particle diameters and snowflake densities can be found in the work of Garrett et al. (2012) and preceding studies (Magono and Nakamura 1965; Locatelli and Hobbs 1974; Barthazy and Schefold 2006; Garrett et al. 2012). It is common to express the terminal velocity of ice particles and snowflakes in terms of the particle Reynolds number and its Davies (or Best) number (Heymsfield and Kajikawa 1987; Mitchell 1996).

Snowflakes may assume a preferred orientation during free fall (Garrett et al. 2015). However, the orientation and rotation of particles with complex shapes are usually time dependant and influenced by the stability of the solid body rotation (Leine et al. 2021; Van Damme et al. 2017). A rotational motion of free falling natural snowflakes has been observed and measured for various Reynolds numbers by Kajikawa (1989).

The translation dynamics of a solid particle of an arbitrary shape in a fluid flow are determined by the net drag force F_d. Its magnitude F_d can be expressed in dimensionless form by means of the drag coefficient defined as

$$C_d = \frac{2F_d}{\rho A_{ref} U^2} \tag{1}$$

where ρ is the fluid density, A_{ref} is a reference area and U is the relative velocity between the particle and the fluid. The drag coefficient C_d is a function of the geometry of the particle, its orientation and the Reynolds number

$$Re = \frac{Ud}{\nu} \tag{2}$$

with a characteristic length scale d and the kinematic viscosity ν.

For a steady incompressible flow around a solid spherical body of diameter d, the drag coefficient is only a function of the Reynolds number. Clift and Gauvin (1970) proposed an equation for the drag coefficient of a solid sphere, given by

$$C_d = \frac{24}{Re}(1 + \beta Re^\eta) + \frac{\gamma}{1 + \delta Re^{-\omega}} \text{ with } Re < 3 \times 10^5, \tag{3}$$

$$\beta = 0.15, \quad \eta = 0.687, \quad \gamma = 0.42,$$
$$\delta = 4.25 \times 10^4, \quad \omega = 1.16. \tag{4}$$

This equation covers a wide range of Reynolds numbers including the Newton regime and up to the sharp drop of the drag coefficient associated with the boundary layer transition to a turbulent state.

The most recent and detailed overview of the existing empirical models for the drag coefficients of irregular particles of various shapes can be found in Roostaee and Vaezi (2022). The drag coefficient of non-spherical particles is often described by using geometric descriptors aimed at representing the complex shape of the particles by a finite number of parameters. The most widely used geometric descriptors of the particle shape are the volume equivalent diameter d_{eq}, the sphericity Φ and the crosswise sphericity $\Phi_\perp$

$$d_{\text{eq}} = \sqrt[3]{\frac{6V}{\pi}}, \quad \varPhi = \frac{\pi d_{\text{eq}}^2}{A}, \quad \varPhi_\perp = \frac{\pi d_{\text{eq}}^2}{4A_\perp}. \tag{5}$$

with the volume V, the surface area A and the area $A_\perp$ of the projection of the body onto the plane normal to the direction of the relative velocity.

Numerous studies about the drag coefficient of irregular particles based on various particle shapes are available in the literature. Among the most advanced models are the correlations of Haider and Levenspiel (1989), Ganser (1993) and Hölzer and Sommerfeld (2008). In all these models, the volume equivalent diameter is used as a length scale, $d = d_{\text{eq}}$ and correspondingly the reference area is defined as $A_{\text{ref}} = \pi d_{\text{eq}}^2/4$. In the models of Haider and Levenspiel (1989) and Ganser (1993), the drag coefficient is expressed in the same form as for spherical particles given in Eq. 3, while the coefficients $\beta, \eta, \gamma, \delta$ and ω are given as functions of the sphericity $\varPhi$.

The model of Hölzer and Sommerfeld (2008) takes into account the fact that the particle sizes can be different in the directions parallel to the fluid stream and normal to it. This dependence is taken into account through the use of the crosswise sphericity, determined in Eq. 5. The correlation proposed by Hölzer and Sommerfeld (2008) reads

$$C_{\text{d}} = \frac{8}{Re\sqrt{\varPhi_\perp}} + \frac{16}{Re\sqrt{\varPhi}} + \frac{3}{\sqrt{Re}\varPhi^{3/4}} + \frac{0.42 \times 10^{0.4(-\log_{10}\varPhi)^{0.2}}}{\varPhi_\perp}. \tag{6}$$

It should be noted that Hölzer and Sommerfeld also suggest a formulation involving the lengthwise sphericity $\varPhi_\parallel$ calculated from the analysis of the particle projections in the planes parallel to the fluid flow direction. However, it has been shown that the correlation given by Eq. 6, based only on the crosswise sphericity $\varPhi_\perp$, agrees very well with experimental data.

In recent studies (Tran-Cong et al. 2004; Loth 2008; Bagheri and Bonadonna 2016; Wang et al. 2018), different empirical correlations for the drag coefficient have been proposed which involve the characteristic geometrical properties of the projected area. The drag force on a blunt body induced by a fluid flow results from the pressure distribution and the viscous shear stresses at the body surface. At high Reynolds numbers, the flow is influenced by flow separation, leading to the formation of a wake behind the body. A snowflake however can be better approximated as a porous body. The force on a porous body or on a body of very complex geometry is influenced also by the flow in the pores. Moreover, the effects associated with the flow through the porous body may lead to a significant change of the outer flow, especially the shape and the type of wake (Castro 1971; Bhattacharyya et al. 2006).

The drag force on a flat porous mesh has been studied theoretically by Taylor (1944). In this model, the plate is represented as an array of local resistances to an incompressible potential flow. This model agrees very well with the experimental data for rather high values of plate porosity. The plate porosity is characterized by the open area ratio, defined as the ratio of the open area to the solid area.

In the study of Cumberbatch (1982), the drag force is modeled for a given pressure jump at the porous plate, where the effect of the flow through the mesh is modeled using Darcy's law. The drag force of the porous plate has been more recently analyzed theoretically by Steiros and Hultmark (2018). The proposed model for the drag coefficient is valid for an arbitrary value of the open area ratio. In addition to the plate resistance, the model of Steiros and Hultmark (2018) also takes into account the crosswise velocities before and after the plate, as well as the effect of the plate porosity on the wake velocity. These models are valid for relatively large Reynolds numbers $Re_{\text{pore}} > 10^3$, based on the pore size (Hoerner 1952).

Heymsfield and Westbrook (2010) proposed a model for estimating the drag coefficient of snowflakes based on the maximum Feret diameter $d_{\max}$ and the area of a projection. The model is an adaption of the model for the drag coefficient of a sphere from Abraham (1970), which is then modified with the Pentland roundness defined as $4A_\perp/\pi d_{\max}^2$ (Pentland 1927).

Tagliavini et al. (2021) performed computational fluid dynamics simulations to predict the drag of single snowflakes and validated the results with experiments conducted with 3D-printed snowflakes. The difficulty associated with the unknown orientation of the particle was accounted for by averaging the drag coefficient from two orientations. In another study, Tagliavini et al. (2021) investigated the wake of falling snowflakes and identified a contribution of the particle pores to the drag.

A rather large number of different existing empirical models for irregular non-spherical particle shapes indicates that the main physical factors influencing the drag coefficients are not yet completely captured in current models, especially for extremely complicated shapes such as those of snowflakes. Moreover, it is not feasible to accurately measure the full three-dimensional shapes of snowflakes, which would be required for the evaluation of most drag models. The lack of reliable and accurate models makes the prediction of the dynamics of clouds of snowflakes in an air flow a very difficult task.

Therefore, the main objective of the present experimental and theoretical study is the development of an approach that allows computation of the trajectories of snowflakes accurately in an airflow, utilizing a statistical approach. For this,

two main steps are performed. In a first step, an experimental reference data set is created for which the drag coefficients of artificial snowflakes of known shape and orientation are determined. Utilizing this data set, existing models for the drag coefficient of irregular particles are evaluated, demonstrating that the main geometrical parameters to be involved in the correlations for reliable predictions should be deduced from the convex hull of the particles.

In a second step, an algorithm for the generation of three-dimensional shape descriptors of snowflakes from two-dimensional images is presented. The statistics of the geometrical parameters of the shapes are determined from the assumption of a random particle orientation. This algorithm has an important practical value, since in many cases in practice only a collection of two-dimensional images is available from the observation of meteorological particles such as snowflakes.

2 Experimental methods

The experimental methods include the design and fabrication of the artificial snowflakes utilized in the experiments, measurements of the terminal velocity of the artificial snowflakes in a water reservoir and post-processing of the data for the estimation of the drag coefficient.

2.1 Digital models of snowflakes and their fabrication

An accurate description of the dynamic of irregular particles, like ice crystals or snowflakes, requires information about the velocity of the air flow, the particle velocity and the exact shape and mass of the particle. All these data are difficult to measure or cannot be measured at all under natural conditions since the air flow is difficult to control and measure, the shape is complex and the mass can usually be measured only after complete melting of the particle.

In this study, three-dimensional digital models of snowflakes are generated in order to create solid artificial snowflakes, produced by additive manufacturing, which are then utilized for the drag force measurements. Furthermore, the digital models are used for the analysis of statistics of their geometrical properties.

The digital models are generated using a code developed by Leinonen et al. (2013). In this code, single ice crystal monomers of various types are stochastically combined to aggregates. Subsequently, these aggregates are subjected to
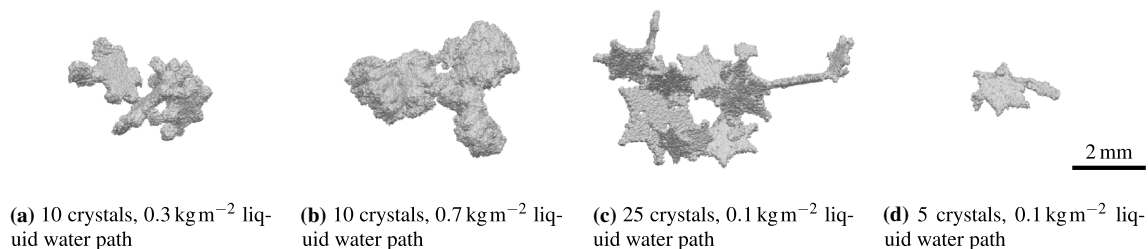
(a) 10 crystals, $0.3\,\mathrm{kg\,m^{-2}}$ liquid water path **(b)** 10 crystals, $0.7\,\mathrm{kg\,m^{-2}}$ liquid water path **(c)** 25 crystals, $0.1\,\mathrm{kg\,m^{-2}}$ liquid water path **(d)** 5 crystals, $0.1\,\mathrm{kg\,m^{-2}}$ liquid water path

Fig. 2 Exemplary digital models of snowflakes showing the variety of the generated snowflakes. While all snowflakes are composed of dendritic ice crystals, the number of monomers and the riming determined by the liquid water path have been varied
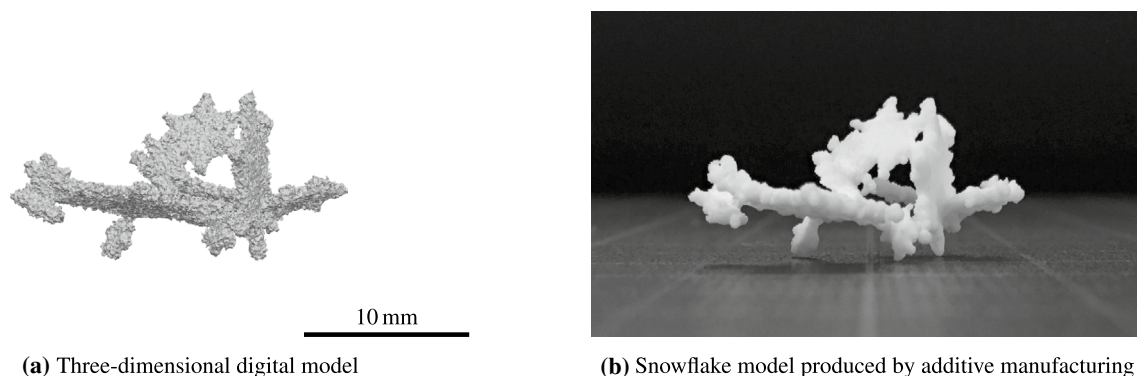
(a) Three-dimensional digital model **(b)** Snowflake model produced by additive manufacturing

Fig. 3 Digital model and manufactured model of an exemplary snowflake composed of 15 dendritic ice crystals subjected to a liquid water path of $0.1\,\mathrm{kg\,m^{-2}}$, which corresponds to only slight riming. The depicted snowflake has been scaled up from its original size by a factor of five

Fig. 4 The experimental setup consisting of a container filled with a glycerol–water mixture, cameras, light sources with diffusing sheets, a temperature sensor and the artificial snowflake. The snowflake is shown here once fixed at the bottom of the container prior to the experiment and once in the field of view of the cameras
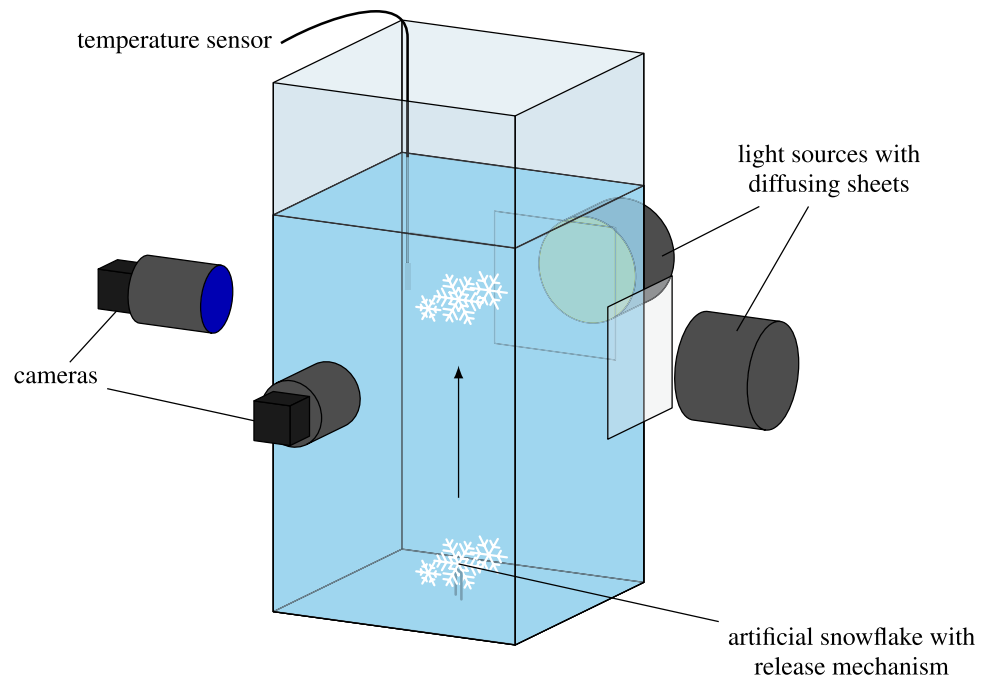
riming. The monomer type, i.e., the shape of the single ice crystals forming the snowflake, the distribution of the monomer sizes and the number of monomers as well as the liquid water path responsible for riming can be specified. More information on the algorithm can be found in the work of Leinonen et al. (2013).

With a focus on aggregates composed of dendritic ice crystals, the number of monomers in a snowflake has been varied from 3 to 25 crystals and the liquid water path covers a range from $0.1\ kg\ m^{-2}$ to $0.7\ kg\ m^{-2}$. The liquid water path can be interpreted as the liquid water content integrated along the path of the snowflake through the air. The utilized values of liquid water paths correspond to a span of barely rimed aggregates up to highly rimed aggregates. These parameter ranges yield a vast variety of different snowflakes of which some examples are shown in Fig. 2. The shapes of the artificial snowflakes appear similar to the natural particles depicted in Fig. 1.

The triangulated digital models are manufactured by selective laser sintering of a polyamide powder. The resolution of the utilized machine is 100 µm in each direction in space. To reach sufficient detail in the printed flake, the digital models were scaled up by a factor of five. A comparison of the upscaled digital model and the manufactured model is depicted in Fig. 3.

2.2 Experimental setup

The experimental setup consists of a container with a water–glycerol mixture, a mechanism to fix and release the artificial snowflakes, two light sources, two cameras and a

temperature sensor. An illustration of the setup is depicted in Fig. 4.

The container is manufactured from acrylic glass to allow optical access from all sides. The inner width and depth are 0.4 m each and the liquid height is 0.6 m. The liquid inside the container is composed of water and glycerol to reach appropriate Reynolds numbers with the artificial snowflakes. The Reynolds numbers were chosen such that they approximately coincide with the Reynolds numbers at the terminal velocities of natural snow. Two different mixing ratios of the two liquids have been used to widen the range of Reynolds numbers. All investigated Reynolds numbers are in the intermediate regime in the order of 10 to 10^3.

In total, 78 different snowflakes have been manufactured, as explained in Sect. 2.1, and tested in multiple runs.

In preparation for the experiment, the snowflake under investigation is fixed at the bottom of the container and the setup is left alone for a minimum period of five minutes. This serves to let the liquid come to rest and minimize the effect of vortices of residual secondary flow in the container on the snowflake trajectory. To start the experiment, the snowflake is released from the bottom of the container and rises upwards due to buoyancy. The snowflake rises through the field of view of two cameras capturing its motion from two orthogonal views; back lighting with two light sources and diffusor plates provide shadowgraphy of the body.

2.3 Post-processing

The videos captured by the two cameras are used to evaluate the snowflake velocity, its orientation and the projected
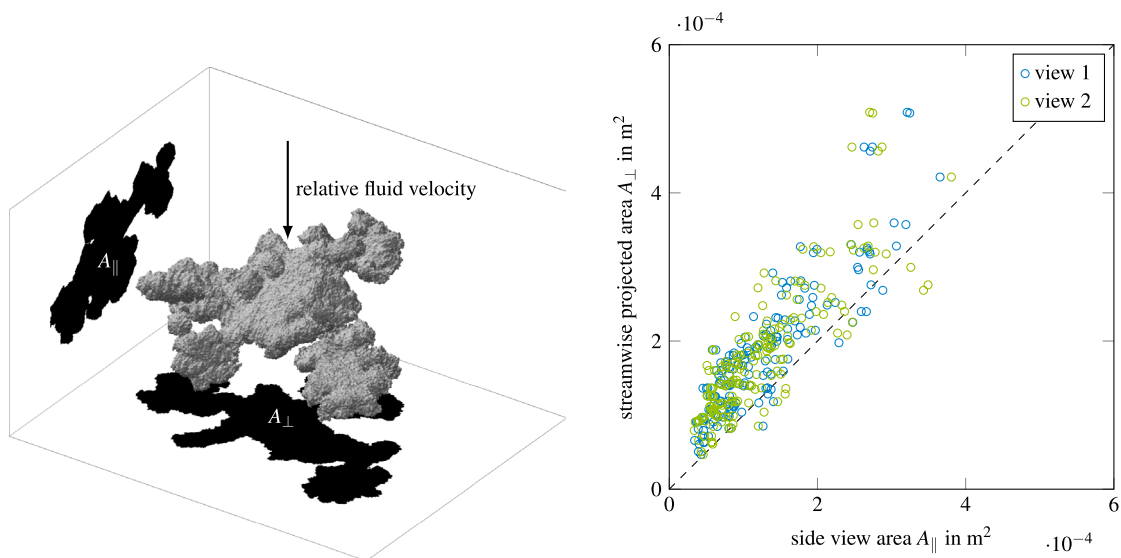
(a) Illustration of the area projected in streamwise direction and an area projected in a direction perpendicular to the flow

(b) Area projected in the direction of flow versus the areas seen from two perpendicular side views

Fig. 5 Characterization of the particle orientation in the flow. Area $A_\perp$ projected on the plane normal to the streamwise direction of the relative fluid flow, as a function of the projected area $A_\parallel$ on a plane parallel to the fluid flow
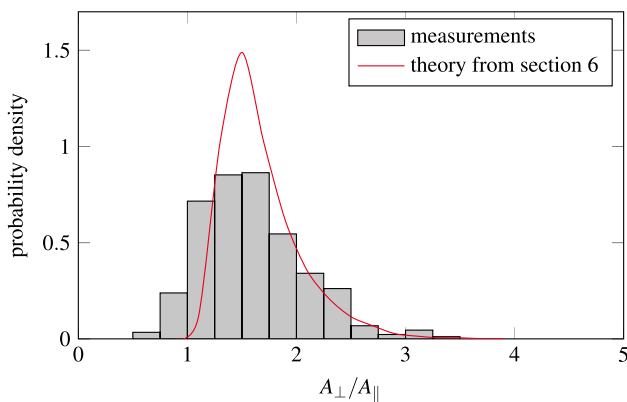

Fig. 6 Probability density function of the ratio $A_\perp/A_\parallel$ of the area $A_\perp$ projected onto a plane normal to the relative velocity vector to the area $A_\parallel$ projected onto a parallel plane. The experimental data are compared with the theoretical predictions from Sect. 6

Fig. 7 Drag coefficients of the snowflakes calculated from the experiments versus the corresponding Reynolds number, which is based on the volume equivalent diameter of the flake. For comparison, the drag coefficient of a sphere at the corresponding Reynolds number calculated from the correlation of Clift and Gauvin (1970) is shown with the solid line

areas. Following the binarization of the video frames, the binary images are post-processed to extract these values.

Due to the constant velocity of the snowflakes within the field of view, an accurate measurement of the rise speed can be evaluated by a linear regression of the snowflake centroid position. The orientation of the snowflake during its rise is evaluated by matching the projection of the digital model with the shape in the binarized video frame. To match the projections, the digital model is stepwise rotated around all three axes. After each step, the projections are compared. A refinement is performed around the orientation with maximum agreement. Given the orientation of the rising
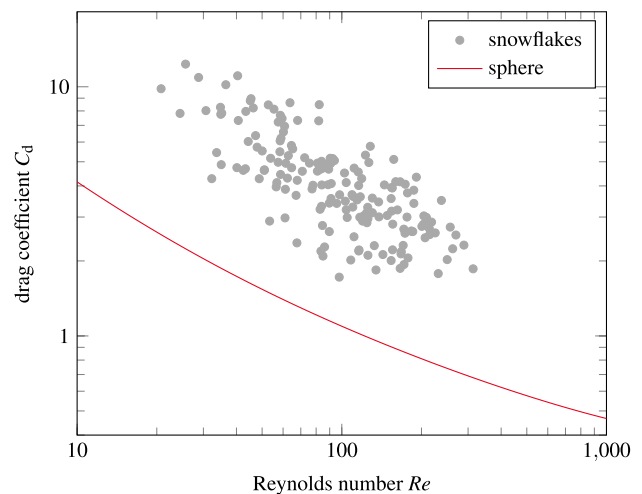
snowflake and the full three-dimensional geometry from the digital model, the area of the snowflake projection in the direction of flow, i.e., as it would be seen from the top, can be evaluated. With this quantity, the crosswise sphericity of the snowflake can be calculated according to Eq. 5.

3 Orientation and drag coefficient of snowflakes

In order to identify a possible preferable orientation of the particles the projected areas $A_\perp$ and $A_\parallel$, defined in Fig. 5a of each particle are compared. The areas $A_\parallel$ are captured by two cameras, providing the front view and the side view of the particle. The dependence of $A_\perp$ on $A_\parallel$ is shown in Fig. 5b. Each symbol in Fig. 5b corresponds to one experiment. The dashed line corresponds to the case $A_\perp = A_\parallel$. These results clearly demonstrate that under stable conditions, the area $A_\perp$ of the preferred particle orientation is close to the maximum projected area of the particle. This indicates that the particles tend to orient such that the area projected in the direction of flow is maximized. Willmarth et al. (1964) showed that the stability of a settling disk also depends on a dimensionless moment of inertia. While snowflakes resemble far more complex shapes, this effect could also affect their orientation.

A normalized histogram of the ratio $A_\perp/A_\parallel$ is shown in Fig. 6. The data from both cameras, the side view and the front view, are used in computing these statistics. The decision to combine these views is based on the assumption that there is not a preferential particle orientation in the parallel plane and the contribution of both of these views to the statistics are equal. Moreover, for many of the investigated snowflakes, a rotation around the vertical axis was observed.

Next, the drag coefficients C_d of the artificial snowflakes are calculated from the force balance accounting for the fact that the terminal snowflake velocity is constant
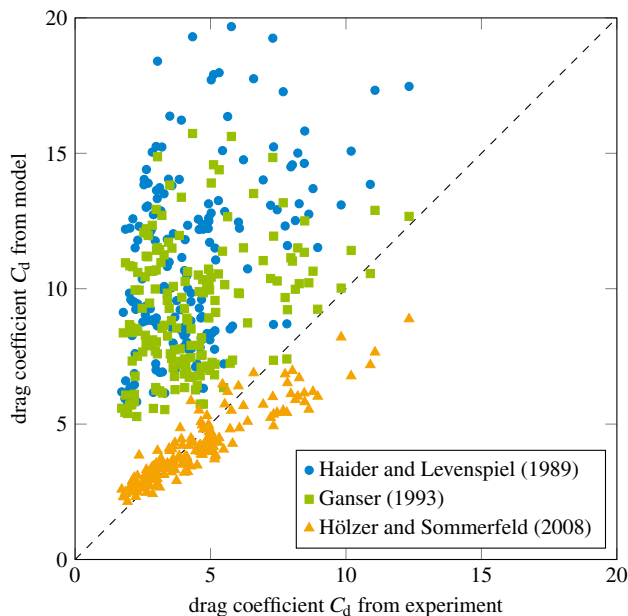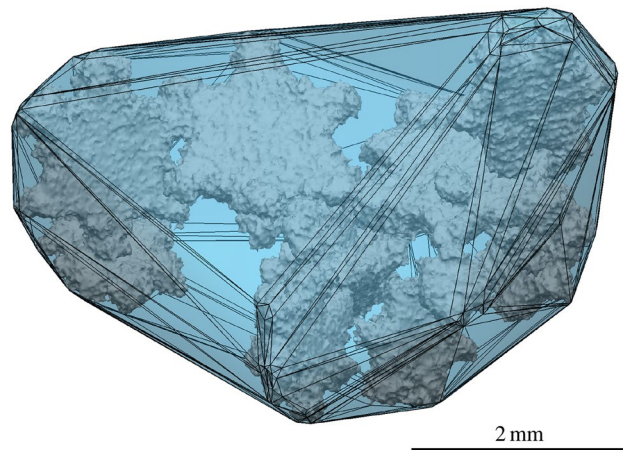

Fig. 9 Digital model of a snowflake and the corresponding convex hull enclosing it. The hypothesis is, that in the investigated Reynolds number range, both bodies experience approximately the same drag force

$$C_d = \frac{2(V\rho - m)g}{\rho A_{\text{ref}} U^2} \qquad (7)$$

where m denotes the snowflake mass, V is its volume, U is the constant terminal velocity of the particle in the resting fluid and g is gravitational acceleration, respectively.

In Fig. 7, the measured data on the drag coefficients, determined using Eq. 7, are shown as a function of the Reynolds number. Here, the reference area for the drag coefficient is given by the projected area of a volume equivalent sphere and the Reynolds number is based on the volume equivalent diameter of the snowflake. The decrease in drag coefficient with increasing Reynolds number can be clearly recognized. Due to the unique snowflake geometry and the large differences in the geometric descriptors, a large scatter can be seen in the data. This scatter highlights the need for correct incorporation of the appropriate geometric descriptors in any model. The drag coefficient of a sphere poses a lower bound for the drag coefficient of the snowflakes.

The knowledge of the exact geometry of the snowflakes allows the computation of all geometric descriptors that are incorporated in the models for drag coefficients existing in literature. The drag coefficients predicted by the models can then be compared with the experimental data. In Fig. 8, the predictions of the models of Haider and Levenspiel (1989), Ganser (1993) and Hölzer and Sommerfeld (2008) are shown in comparison with the experimental data. The dashed line corresponds to perfect agreement. Among these models, only the predictions of the model of Hölzer and Sommerfeld (2008) agree well with the experiments.

Fig. 8 Comparison of the drag coefficient predicted by the models of Haider and Levenspiel (1989), Ganser (1993) and Hölzer and Sommerfeld (2008) and the drag coefficient in the experiment

4 Convex hull approximation of the particle shape

The main idea of the newly proposed approach is in the representation of the snowflake as a porous body, whose shape is a convex hull of the particle. An example of such a porous body is shown in Fig. 9. The drag coefficient of the snowflake can then be modeled based on the correlation for the drag coefficient of the much simpler geometry of the convex hull shape.

In the experiments conducted in the present study, the Reynolds number of the particle is in the range $10 < Re < 10^3$, which corresponds to real snow conditions. The estimated Reynolds number of the pore is $Re_{pore} \ll 10^2$, since the intrinsic velocity of the fluid in the pores is much smaller than the relative velocity of fluid in the outer flow. Viscous effects therefore play an important role in the problem. The permeability κ of the porous convex hull of porosity φ can be roughly estimated by the Carman-Kozeny equation (Crowe 2005)

$$\kappa = \frac{\varphi^3}{180(1-\varphi)^2} d_{pore}^2, \tag{8}$$

where d_{pore} is a typical pore size.

The pressure difference Δp at the particle surface can be estimated from the Bernoulli equation neglecting suction in the porous body

$$\Delta p \sim \frac{1}{2} \rho U^2. \tag{9}$$

The average fluid velocity u through the porous body can now be estimated from Darcy's law

$$u = \frac{\kappa \Delta p}{\nu \rho d} = U \frac{d_{pore}^2 \varphi^3}{360 d^2 (1-\varphi)^2} Re. \tag{10}$$

Estimations for the set of parameters of a snowflake and the flow conditions, $d_{pore}/d \sim 0.3$, $\varphi \sim 0.5$ and $Re \sim 10^3$, yield the value of the upper bound for the average fluid velocity entering the porous body $u/U \sim 10^{-1}$. The corresponding reduction of the pressure at the part of the particle surface exposed to the outer fluid flow is $\rho u^2/2 \ll \Delta p$. The effect of the suction of the flow on the value of the drag coefficient is therefore negligibly small. Under these conditions, the drag coefficient of the snowflake should be well approximated by the drag coefficient of its convex hull. These considerations are in qualitative agreement with the results of Tagliavini et al. (2021), who found a drag contribution of the pores of dendritic ice crystals that was attributed to a thickening of the boundary layer, which reduced the flow through the pores. A similar effect was observed by Cummins et al. (2018) for the pappus of a dandelion.
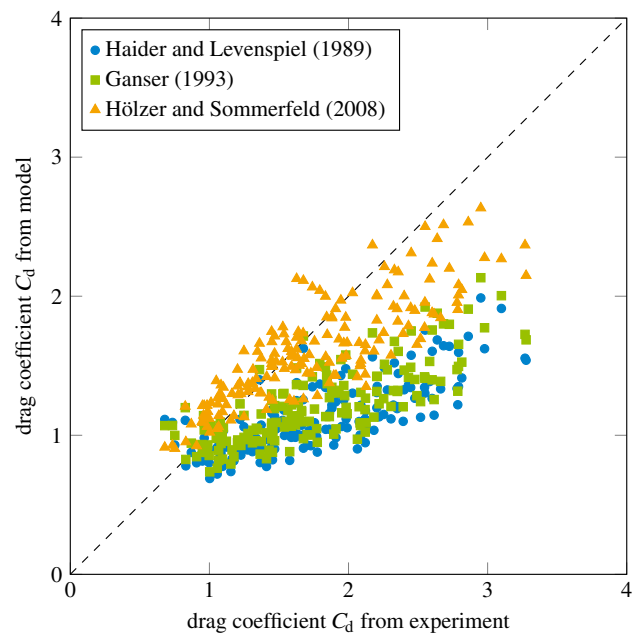

Fig. 10 Comparison of the models of Haider and Levenspiel (1989), Ganser (1993) and Hölzer and Sommerfeld (2008) based on the three-dimensional convex hull geometry as an input with the drag coefficients from the experiment

It should be noted that the effects of permeability can be significant at very high Reynolds numbers or for highly porous snowflakes. This issue will require a further generalization of the developed model, which is out of scope of the present study.

In Fig. 10, the theoretical predictions of the drag coefficients using the models of Haider and Levenspiel (1989), Ganser (1993) and Hölzer and Sommerfeld (2008) applied to the convex hull are shown in comparison to the experimental data. The straight dashed line corresponds to perfect agreement. In comparison to Fig. 8, a significant improvement in the predictions of the models of Haider and Levenspiel (1989) and Ganser (1993) can be seen. Furthermore, the predictions of the Hölzer and Sommerfeld (2008) model improved as well.

The results of this study indicate that for a reliable modeling of the drag coefficient of particles of complex shape, like snowflakes, the choice of a reliable empirical model with a proper shape simplification is crucial. The results of the present study suggest the usage of the model of Hölzer and Sommerfeld (2008) in combination with the convex hull approach. This approach is valid when the flow through the porous body is negligibly small.
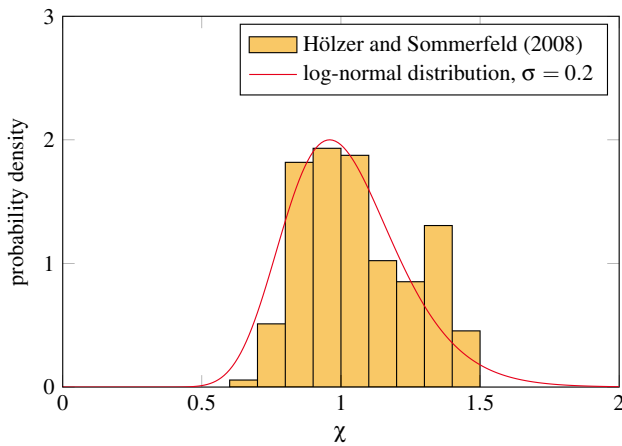
Fig. 11 Distribution of the values of χ representing the ratio of the measured and the average modeled drag coefficients. The data are approximated by a log-normal distribution given by Eq. 12

5 Generation of snow clouds for computations

Numerical simulations of snow clouds require algorithms to generate representative particles of the cloud. The method described in this section aims to introduce the natural variation of snowflakes in artificial snow clouds.

The scatter of the data presented in the previous section reflects the fact that dynamic effects associated with the real shape of the particle also play a role. To account for this effect when generating snow clouds for computations, a coefficient

$$\chi \equiv \frac{C_{d,\,\text{experiment}}}{C_{d,\,\text{model}}} \tag{11}$$

is defined. This coefficient describes the ratio of the drag coefficient of a real particle (obtained from the measurements) and that of a simplified particle geometry represented by its convex hull. In this study, the values of the coefficient χ are calculated using the model of Hölzer and Sommerfeld (2008) for the estimation of $C_{d,\,\text{model}}$. In Fig. 11, the probability density function of the values of the coefficient χ is compared with the log-normal distribution

$$f(\chi) = \frac{1}{\sqrt{2\pi}\sigma\chi} \exp\left(-\frac{\ln^2 \chi}{2\sigma^2}\right) \tag{12}$$

where the standard deviation parameter $\sigma = 0.2$ is obtained through a fit to the obtained data.

Therefore, the drag coefficients $C_{d,i}$ of the i-th particle in a cloud of real snowflakes of various shapes can be generated accounting for the mean value $C_{d,\,\text{model}}$, which is predicted using the corresponding convex hull and the

stochastic part associated with the variety of the particle forms

$$C_{d,i} = \chi_i C_{d,\,\text{model}}, \quad \chi_i = \exp\left[\sqrt{2}\sigma\,\text{erf}^{-1}(2\mathcal{R}_i - 1)\right], \tag{13}$$

where $\mathcal{R}$ is a random number between 0 and 1 and $\text{erf}^{-1}(\cdot)$ is the inverse error function. Using this method, representative particles can be generated for use in numerical simulations of snowflake trajectories.

6 Prediction of the drag coefficient from two-dimensional projections

It is obvious that not all details of the shapes of real snowflakes can be taken into account in computer simulations of a snow cloud. Only the main parameters of the particles governing the particle dynamics in an air flow can be considered. Besides the snowflakes mass, these parameters include those determined in Eq. 5. For the estimation of the drag force, the equivalent diameter of the convex hull of the particle and its sphericity must be known.

In most in-flight or ground measurements, only a single photograph of each snowflake is available. The geometry of a single projection of a complex three-dimensional particle is not sufficient for the reconstruction of a three-dimensional convex hull. Even a set of images of a single particle does not enable the reconstruction of the exact three-dimensional shape of the particle. In order to extract information about the quantities relevant for trajectory calculations from two-dimensional images, the simplified shapes of convex hulls are analyzed. The focus of this analysis is to determine whether some correlations can be identified for the particle convex hull diameters and sphericities. A comparison of the correlation coefficients of various two-dimensional descriptors with the volume equivalent diameter and the sphericity results in the following two quantities used for the correlations: The area equivalent diameter to approximate the volume equivalent diameter and the Cox roundness (Cox 1927) to approximate the sphericity. These two-dimensional descriptors are defined as

$$d_{2D} = \sqrt{\frac{4A_p}{\pi}} \text{ and } \Phi_{2D} = \frac{4\pi A_p}{P^2} \tag{14}$$

with the projected area A_p and the perimeter P of the projection.

In the following subsections, a simplified model of a convex hull is developed and the relation of its three-dimensional shape descriptors to the parameters of its two-dimensional projection is derived. Subsequently, a complementing
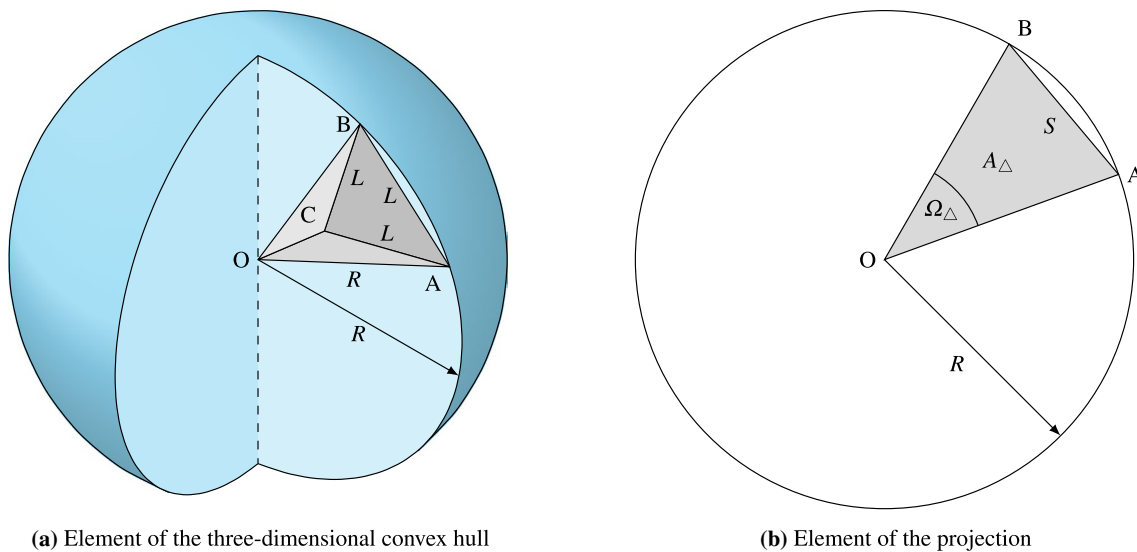
(a) Element of the three-dimensional convex hull

(b) Element of the projection

Fig. 12 Models of a simple convex hull and its projection. **a** a three-dimensional element of the convex hull, approximated by a tetrahedron, **b** an element of the projection

Monte Carlo experiment is conducted with a data set of artificial snowflakes and their projections. This enables the estimation of the three-dimensional properties of the convex hull from its two-dimensional projection.

6.1 Theoretical construction of convex particles

Consider an element of a simplified convex shape as a tetrahedron, shown in Fig. 12a, with the four vertices A, B, C and O. The vertices A, B and C are at the surface of a sphere of the radius R with the center at the vertex O. The triangular face ABC is an equilateral triangle of the length $L = lR$, with the dimensionless shape parameter l, which determines the convex shape sphericity. The characteristic length L determines the variety of the shapes of the geometric body consisting of multiple tetrahedrons representing the convex hull.

The volume of the tetrahedron $V_\diamond$, the area of its outer face $A_\diamond$ and the solid angle $\Omega_\diamond$, which is defined as the area of the segment of a unit sphere the tetrahedron covers, are determined from the geometrical considerations

$$V_\diamond = \frac{R^3}{12} l^2 \sqrt{3 - l^2} \text{ with } l < \sqrt{3} \tag{15}$$

$$A_\diamond = \frac{\sqrt{3}}{4} l^2 R^2 \tag{16}$$

$$\Omega_\diamond = 4 \arctan \sqrt{\tan \frac{3\theta}{4} \tan^3 \frac{\theta}{4}} \text{ with } \theta = 2 \arcsin \frac{l}{2}, \tag{17}$$

respectively. The average number of these tetrahedrons in the convex hull body can be estimated accounting for the solid angle of a sphere 4π

$$N_\diamond = \frac{4\pi}{\Omega_\diamond} \tag{18}$$

Now the equivalent diameter and the sphericity of the body can be estimated as

$$d_{eq}(l) = \sqrt[3]{\frac{6 V_\diamond N_\diamond}{\pi}} = R \sqrt[3]{\frac{2 l^2 \sqrt{3 - l^2}}{\Omega_\diamond(l)}} \tag{19}$$

$$\Phi(l) = \frac{\pi d_{eq}^2}{A_\diamond N_\diamond} = \sqrt[3]{\frac{4 \Omega_\diamond(l)(3 - l^2)}{l^2 \sqrt{27}}}. \tag{20}$$

Consider now a projection of the convex hull, as shown in Fig. 12b. The element of the projection can be approximated by an isosceles triangle with the legs R and the base $S = Rs$ with s being the dimensionless ratio of the base to the radius. The area $A_\triangle$, the vertex angle $\Omega_\triangle$ and the average number $N_\triangle$ of the triangles in the circle of the radius R are

$$A_\triangle = \frac{R^2 s}{2} \sqrt{1 - \frac{s^2}{4}} \tag{21}$$

$$\Omega_\triangle = 2 \arcsin \frac{s}{2} \tag{22}$$

$$N_\triangle = \frac{2\pi}{\Omega_\triangle} \tag{23}$$
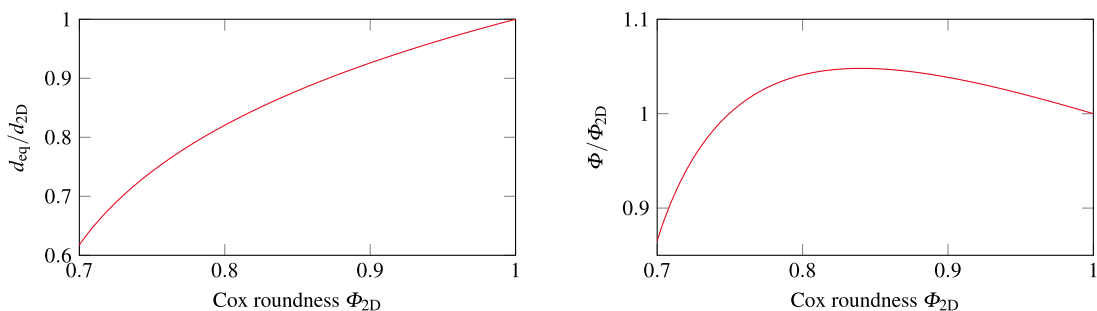
(a) Diameter ratio d_{eq}/d_{2D} as a function of the Cox roundness Φ_{2D}

(b) Ratio Φ/Φ_{2D} as a function of the Cox roundness Φ_{2D}

Fig. 14 Theoretically predicted correlations of convex hull properties with the projection properties. Both ratios of the three-dimensional properties to the two-dimensional property depend on the Cox roundness

Now the equivalent diameter of the projection and the Cox roundness can be estimated as

$$d_{2D}(s) = \sqrt{\frac{4A_\triangle N_\triangle}{\pi}} = R\frac{\sqrt{s}\sqrt[4]{4-s^2}}{\sqrt{\arcsin\frac{s}{2}}} \tag{24}$$

$$\Phi_{2D}(s) = \frac{4\pi A_\triangle N_\triangle}{(sRN_\triangle)^2} = \frac{2}{s}\sqrt{1-\frac{s^2}{4}}\arcsin\frac{s}{2} \tag{25}$$

Finally, the relation between the characteristic lengths L and S can be determined by considering the projection of the characteristic equilateral triangle ABC of the side length L on an arbitrary plane normal to the triangle plane, as shown in Fig. 13. The average length of the projection is estimated using the assumption that the inclination angle α is distributed uniformly between 0 and $\pi/6$.
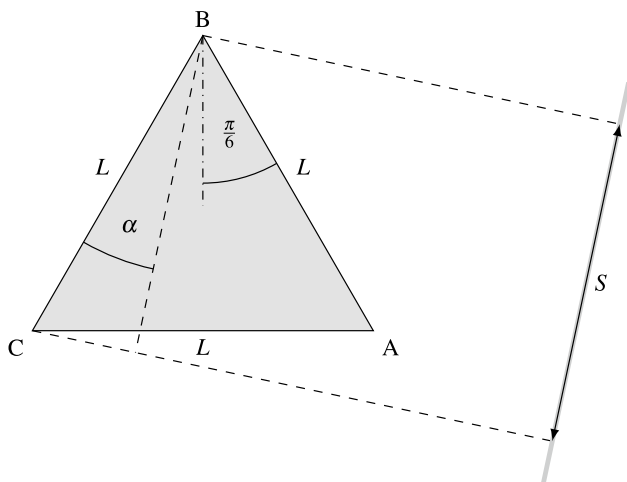
Fig. 13 Projection of the triangle ABC on an arbitrary plane. Definition of the inclination angle α and the projection length S

$$S = \frac{6}{\pi}\int_0^{\pi/6} L\cos\alpha\, d\alpha = \frac{3L}{\pi}, \text{ i.e., } s = \frac{3l}{\pi} \tag{26}$$

The integration limits are determined accounting for the symmetry of the triangle ABC.

The theoretically predicted ratios Φ/Φ_{2D} and d_{eq}/d_{2D} are shown in Fig. 14 as functions of the Cox roundness Φ_{2D}. These correlations can be used for the modeling of the distributions of d_{eq} and Φ if the values of d_{2D} and Φ_{2D} are known from the image processing of the particle convex hull.

The predicted Cox roundness of the projection is in the range $\Phi_{2D} \in [0.66, 1]$. The approximation is not applicable to cases where the Cox roundness of the projection is smaller than 0.66. Therefore, this model can be used if the number of projections with $\Phi_{2D} < 0.66$ is much smaller than the total number of the images and therefore the cases which cannot be interpreted using present approximation is negligibly small.

6.2 Monte Carlo simulations of two-dimensional projections of digital snowflakes

In order to evaluate the shape distribution of snowflakes, a data set of three-dimensional and two-dimensional descriptors is developed for the digital snowflake models. A Monte Carlo simulation is performed based on this data set to find a correlation for the relevant parameters of the three-dimensional convex hull and the parameters of the two-dimensional convex hulls of the projections.

An ensemble of 102 three-dimensional digital snowflakes are generated and analyzed. For each snowflake, 100 two-dimensional projections of random orientations are produced. This procedure yields 10200 projections of which correlations between equivalent diameter and projected diameter as well as sphericity and Cox roundness are extracted.
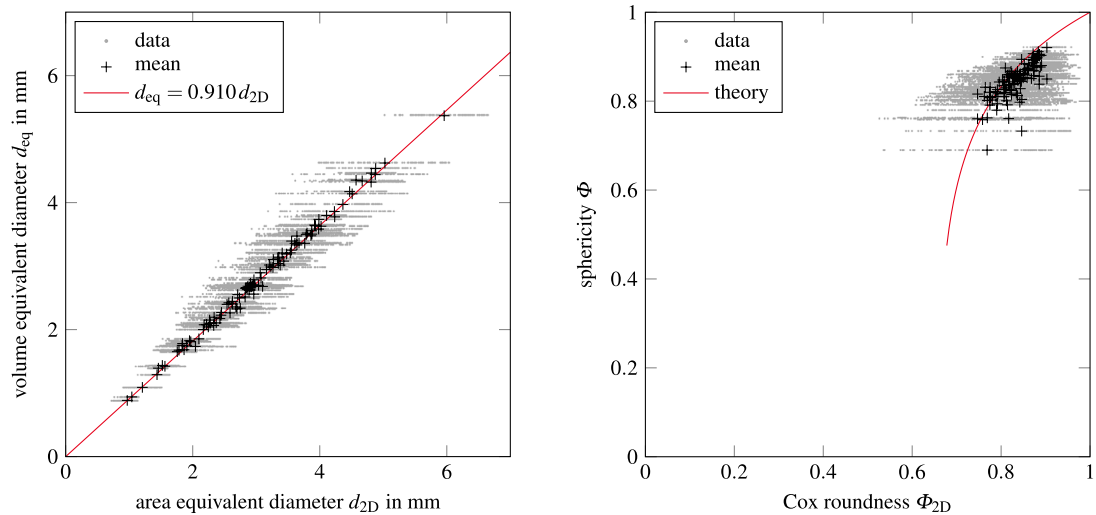
(a) Equivalent diameter d_{eq} of the convex hull as a function of d_{2D} of its arbitrary projections

(b) Sphericity Φ of the convex hull as a function of the Cox roundness Φ_{2D}

Fig. 15 Evaluation of the main geometrical properties of the shapes of the digital snowflakes from the Monte Carlo computational simulations. The plus signs in each figure correspond to the mean of the two-dimensional descriptor of the 100 projections for each snowflake

In Fig. 15a, the values of the convex hull volume equivalent diameter from the simulations are shown as a function of the area equivalent diameters d_{2D} of the corresponding projections. The average values of d_{eq} and d_{2D} correlate best as $\langle d_{eq} \rangle \approx 0.910 \langle d_{2D} \rangle$, which indicates that the particle convex hulls are similar and their shapes do not change significantly with particle size. As illustrated in Fig. 14a, it was shown that the diameter ratio depends only on the particle sphericity. This means that the ratio $\langle d_{eq} \rangle / \langle d_{2D} \rangle \approx 0.910$, obtained from the Monte Carlo simulations, is not a universal constant, but depends on the distribution of the particle sphericities.

In Fig. 15b, the sphericity of the convex hull of the digitally generated snowflakes is shown as a function of the Cox roundness of an arbitrary projection in comparison with the theoretical prediction, expressed in Eqs. 20, 25 and 26. The agreement between the simulations and the theory is rather good within the investigated sphericity range, which is relevant for the generated snowflakes.

The developed correlations can be used to estimate the volume equivalent diameter and the sphericity of the convex hull of a particle from the area equivalent diameter and the Cox roundness of the two-dimensional convex hull of a projection of the particle. These pseudo-three-dimensional descriptors can then be used to estimate the drag coefficient of the body.

Finally, the orientation of a free snowflake in a flow can be determined. The difficulty is in the estimation of the possible areas $A_\perp$ from the statistics of the particle projections. The largest possible projected area of a convex hull is equal to the projected area of the circumscribed sphere

of the radius R. Therefore, the ratio of the areas can be estimated as $A_\perp / A_\parallel \sim 4R^2 / d_{eq}^2$. The value of $4R^2 / d_{eq}^2$ can be estimated from the theoretical considerations, Eqs. 19 and 25 as a function of the Cox roundness of the projection Φ_{2D}. The values for the digitally generated snowflakes are computed and then compared with the experimental data in Fig. 6. The agreement is rather good for the larger values. Some over-prediction of the theory for the values $A_\perp \approx A_\parallel$ is explained mainly by the fact that in a few observed cases $A_\perp$ was slightly smaller than $A_\parallel$, which is
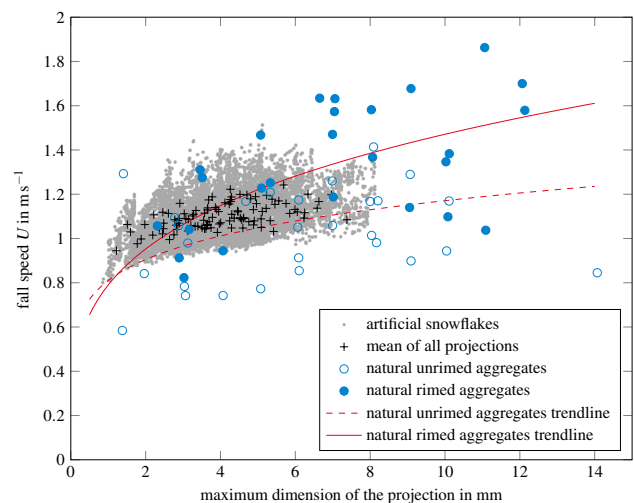

Fig. 16 Comparison of fall speeds obtained for the artificial snowflake data set with the data set of Locatelli and Hobbs (1974) gathered with natural snow. The latter data set contains aggregates of dendrites and aggregates of radiating assemblages of dendrites both unrimed and densely rimed

not accounted for in the theory. On the other hand, for all the cases where $A_\perp \approx A_\parallel$ the possible error in the prediction will be small, since the areas are similar.

As a final validation, the correlation between fall speed and maximum dimension of the snowflake projection is tested. With these quantities, the synthetic data can be compared with measurements obtained with natural snow. Since literature on the drag coefficients of natural snowflakes is sparse, the fall speed is used as an indirect measure of drag to validate the data. Locatelli and Hobbs (1974) measured the fall speed of snowflakes and suggested correlations for the mass-size relationship of these snowflakes. Locatelli and Hobbs shielded the falling snowflakes in a tower to minimize the influence of the wind; however, data sets of natural snowflakes can be subjected to the effects of turbulence, which are discussed in detail by Nemes et al. (2017) and Li et al. (2021) and may lead to increased scatter in collected data. These effects are not accounted for in the drag modeling in the present study and did not occur in the experiments due to the resting fluid. Figure 16 shows the modeled terminal velocity as a function of the maximum dimension of its projection in comparison with the data of Locatelli and Hobbs (1974). The modeled values are computed by solving the equation of motion for each snowflake with the drag coefficient calculated based on the projection of the snowflake convex hull and the mass obtained from the mass-size relationship for rimed aggregates of dendrites given by Locatelli and Hobbs (1974). Thus, only information that can be drawn from two-dimensional projections of the snowflakes is used. This is done for each of the more than 10000 generated projections. In addition, the plot shows the mean value of all the projections created for each snowflake. The comparison shows a good agreement of the artificial snowflakes with the natural snowflakes. Both the artificial and the natural data set exhibit a significant scatter with comparable variability in the size range covered by the artificial flakes. This is attributed to the large variety of snowflake geometries. The overall trend and magnitude of the data are comparable, which confirms that the generated snowflakes were representative of natural snow and that the calculation of the drag coefficient from the convex hull from a two-dimensional projection yields satisfactory results. However, the data shown in Fig. 16 represent only the simplest possible validation with data for natural snow. Further efforts are required for the model validation under more complicated flow conditions. It should be noted that the snowflake mass has a significant influence on the fall speed. To guarantee consistency of mass and fall speed, both are taken from the same source.

7 Summary

The work presented comprises the modeling of drag coefficients of snowflakes and the reconstruction of snowflake geometries from its projections. An experimental investigation of the drag coefficient of digitally generated snowflakes has been conducted. An approximation of the snowflake geometry with its convex hull has been proposed and it has been shown that the predictions of the drag force can be improved significantly with this approach. Furthermore, a method for the generation of synthetic snow clouds with representative drag coefficients for numerical calculations has been presented. Finally, a theory and a corresponding Monte Carlo simulation have been described, which enable the estimation of the three-dimensional parameters relevant for drag calculations from two-dimensional projections of snowflakes.

Declarations

Conflict of interest The authors have no competing interests to declare that are relevant to the content of this article.

Ethical approval Not applicable.

References

Abraham FF (1970) Functional dependence of drag coefficient of a sphere on Reynolds number. Phys Fluids 13(8):2194. https://doi.org/10.1063/1.1693218

Bagheri G, Bonadonna C (2016) On the drag of freely falling non-spherical particles. Powder Technol 301:526–544. https://doi.org/10.1016/j.powtec.2016.06.015

Barthazy E, Schefold R (2006) Fall velocity of snowflakes of different riming degree and crystal types. Atmos Res 82(1–2):391–398. https://doi.org/10.1016/j.atmosres.2005.12.009

Bhattacharyya S, Dhinakaran S, Khalili A (2006) Fluid motion around and through a porous cylinder. Chem Eng Sci 61(13):4451–4461. https://doi.org/10.1016/j.ces.2006.02.012

Castro I (1971) Wake characteristics of two-dimensional perforated plates normal to an air-stream. J Fluid Mech 46(3):599–609. https://doi.org/10.1017/S0022112071000727

Clift R, Gauvin WH (1970) The motion of particles in turbulent gas streams. In: Chemeca '70: A conference convened by the Australian National Committee of the Institution of Chemical Engineers and the Australian Academy of Science pp 14–28

Cox EP (1927) A method of assigning numerical and percentage values to the degree of roundness of sand grains. J Paleontol 1(3):179–183

Crowe CT (2005) Multiphase flow handbook. CRC Press, Boca Raton

Cumberbatch E (1982) Two-dimensional flow past a mesh. Quart J Mech Appl Math 35(3):335–344. https://doi.org/10.1093/qjmam/35.3.335

Cummins C, Seale M, Macente A, Certini D, Mastropaolo E, Viola IM, Nakayama N (2018) A separated vortex ring underlies the flight of the dandelion. Nature 562(7727):414–418. https://doi.org/10.1038/s41586-018-0604-2

Currie T, Struk P, Tsao JC, Fuleki D, Knezevici D (2012) Fundamental study of mixed-phase icing with application to ice crystal accretion in aircraft jet engines. In: 4th AIAA atmospheric and space environments conference, p 3035, https://doi.org/10.2514/6.2012-3035

Farzaneh M (2008) Atmospheric icing of power networks. Springer Science and Business Media, Berlin

Ganser GH (1993) A rational approach to drag prediction of spherical and nonspherical particles. Powder Technol 77(2):143–152. https://doi.org/10.1016/0032-5910(93)80051-B

Garrett TJ, Fallgatter C, Shkurko K, Howlett D (2012) Fall speed measurement and high-resolution multi-angle photography of hydrometeors in free fall. Atmos Meas Tech 5(11):2625–2633. https://doi.org/10.5194/amt-5-2625-2012

Garrett TJ, Yuter SE, Fallgatter C, Shkurko K, Rhodes SR, Endries JL (2015) Orientations and aspect ratios of falling snow. Geophys Res Lett 42(11):4617–4622. https://doi.org/10.1002/2015GL064040

Grazioli J, Ghiggi G (2021) MASCDB, a database of images, descriptors and microphysical properties of individual snowflakes in free fall. Sci Data. https://doi.org/10.5281/zenodo.5709832

Haider A, Levenspiel O (1989) Drag coefficient and terminal velocity of spherical and nonspherical particles. Powder Technol 58(1):63–70. https://doi.org/10.1016/0032-5910(89)80008-7

Heymsfield AJ, Kajikawa M (1987) An improved approach to calculating terminal velocities of plate-like crystals and graupel. J Atmos Sci 44(7):1088–1099. https://doi.org/10.1175/1520-0469(1987)044<1088:AIATCT>2.0.CO;2

Heymsfield AJ, Westbrook CD (2010) Advances in the estimation of ice particle fall speeds using laboratory and field measurements. J Atmos Sci 67(8):2469–2482. https://doi.org/10.1175/2010JAS3379.1

Hoerner SF (1952) Aerodynamic properties of screens and fabrics. Text Res J 22(4):274–280. https://doi.org/10.1177/004051755202200405

Hölzer A, Sommerfeld M (2008) New simple correlation formula for the drag coefficient of non-spherical particles. Powder Technol 184(3):361–365. https://doi.org/10.1016/j.powtec.2007.08.021

Kajikawa M (1989) Observation of the falling motion of early snowflakes. J Meteorol Soc Jpn Ser II 67(5):731–738. https://doi.org/10.2151/jmsj1965.67.5_731

Köbschall K, Breitenbach J, Roisman IV, Tropea C, Hussong J (2022) Geometric descriptors for the prediction of snowflake drag. https://doi.org/10.48328/tudatalib-960

Langleben MP (1954) The terminal velocity of snowflakes. Q J R Meteorol Soc 80(344):174–181. https://doi.org/10.1002/qj.49708034404

Leine RI, Capobianco G, Bartelt P, Christen M, Caviezel A (2021) Stability of rigid body motion through an extended intermediate axis theorem: application to rockfall simulation. Multibody Syst Dyn. https://doi.org/10.1007/s11044-021-09792-y

Leinonen J, Moisseev D, Nousiainen T (2013) Linking snowflake microstructure to multi-frequency radar observations. J Geophys Res Atmos 118(8):3259–3270. https://doi.org/10.1002/jgrd.50163

Li C, Lim K, Berk T, Abraham A, Heisel M, Guala M, Coletti F, Hong J (2021) Settling and clustering of snow particles in atmospheric turbulence. J Fluid Mech. https://doi.org/10.1017/jfm.2020.1153

Locatelli JD, Hobbs PV (1974) Fall speeds and masses of solid precipitation particles. J Geophys Res 79(15):2185–2197. https://doi.org/10.1029/JC079i015p02185

Loth E (2008) Drag of non-spherical solid particles of regular and irregular shape. Powder Technol 182(3):342–353. https://doi.org/10.1016/j.powtec.2007.06.001

Magono C, Nakamura T (1965) Aerodynamic studies of falling snowflakes. J Meteorol Soc Jpn Ser II 43(3):139–147. https://doi.org/10.2151/jmsj1965.43.3_139

Mitchell DL (1996) Use of mass- and area-dimensional power laws for determining precipitation particle terminal velocities. J Atmos Sci 53(12):1710–1723. https://doi.org/10.1175/1520-0469(1996)053<1710:UOMAAD>2.0.CO;2

Nemes A, Dasari T, Hong J, Guala M, Coletti F (2017) Snowflakes in the atmospheric surface layer: observation of particle-turbulence dynamics. J Fluid Mech 814:592–613. https://doi.org/10.1017/jfm.2017.13

Pentland A (1927) A method of measuring the angularity of sands. Proc Trans R Soc Can 21(3):43

Pilcher H (2013) The great white lie: what snowflakes really look like. New Sci 220(2948–2949):70–71. https://doi.org/10.1016/S0262-4079(13)62968-1

Roostaee A, Vaezi M (2022) Developing a standard platform to predict the drag coefficient of irregular shape particles. Powder Technol 395:314–337. https://doi.org/10.1016/j.powtec.2021.09.037

Saunders C, Peck S (1998) Laboratory studies of the influence of the rime accretion rate on charge transfer during crystal/graupel collisions. J Geophys Res Atmos 103(D12):13949–13956. https://doi.org/10.1029/97JD02644

Steiros K, Hultmark M (2018) Drag on flat plates of arbitrary porosity. J Fluid Mech. https://doi.org/10.1017/jfm.2018.621

Tagliavini G, McCorquodale M, Westbrook C, Corso P, Krol Q, Holzner M (2021) Drag coefficient prediction of complex-shaped snow particles falling in air beyond the Stokes regime. Int J Multiph Flow 140:103652. https://doi.org/10.1016/j.ijmultiphaseflow.2021.103652

Tagliavini G, McCorquodale M, Westbrook C, Holzner M (2021) Numerical analysis of the wake of complex-shaped snow particles at moderate Reynolds number. Phys Fluids 33(10):105103. https://doi.org/10.1063/5.0064902

Taylor G (1944) Air resistance of a flat plate of very porous material. Aeronaut Res Counc Rep Mem 2236:159–162

Tran-Cong S, Gay M, Michaelides EE (2004) Drag coefficients of irregularly shaped particles. Powder Technol 139(1):21–32. https://doi.org/10.1016/j.powtec.2003.10.002

Van Damme L, Mardešić P, Sugny D (2017) The tennis racket effect in a three-dimensional rigid body. Phys D 338:17–25. https://doi.org/10.1016/j.physd.2016.07.010

Wang Y, Zhou L, Wu Y, Yang Q (2018) New simple correlation formula for the drag coefficient of calcareous sand particles of highly irregular shape. Powder Technol 326:379–392. https://doi.org/10.1016/j.powtec.2017.12.004

Willmarth WW, Hawk NE, Harvey RL (1964) Steady and unsteady motions and wakes of freely falling disks. Phys Fluids 7(2):197. https://doi.org/10.1063/1.1711133